ACS OMEGA

Open Access

http://pubs.acs.org/journal/acsodf

Article

Liquid Redox Probe-Free Plastic Antibody Development for Malaria Biomarker Recognition

Juliane Corrêa Glória,◆ Daniela S. Oliveira,◆ Ariamna Dip Gandarilla, Yonny Romaguera Barcelay, Luis André Morais Mariúba, Paulo Afonso Nogueira, Walter Ricardo Brito,* and Felismina T. C. Moreira*

Cite This: *ACS Omega* 2024, 9, 33130−33139

Read Online

ACCESS | Metrics & More | Article Recommendations | Supporting Information

ABSTRACT: Malaria is a major public health challenge worldwide and requires accurate and efficient diagnostic methods. Traditional diagnostic approaches based on antigen−antibody interactions are associated with ethical and economic concerns. Molecularly imprinted polymers (MIPs) offer a promising alternative by providing a complementary polymer structure capable of selectively binding target molecules. In this study, we developed a liquid, redox-probe-free, MIP-based electrochemical biosensor to detect the *Plasmodium falciparum* malaria marker histidine-rich protein (HRP2) at the point-of-care (PoC). The imprinting phase consists of the electropolymerization of the monomer methylene blue (MB) in the presence of the target protein HRP2 at the working electrode (WE) of the modified carbon screen printed electrode (C-SPE). Subsequent removal of the protein with proteinase K and oxalic acid yielded the MIP material. The sensor assembly was monitored by cyclic voltammetry (CV), Raman spectroscopy and scanning electron microscopy (SEM). The analytical performance of the biosensor was evaluated by square-wave voltammetry (SWV) using calibration curves in buffer and serum with a detection limit of 0.43 ± 0.026 pg mL^{-1}. Selectivity studies showed minimal interference, indicating a highly selective assay. Overall, our approach to detect the HRP2 infection marker offers simplicity, cost-effectiveness and reliability. In particular, the absence of a redox solution simplifies detection, as the polymer itself is electroactive and exhibits oxidation and reduction peaks.

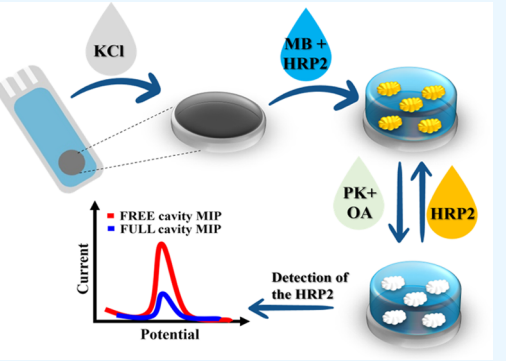

1. INTRODUCTION

Malaria remains a serious health problem in the tropical and subtropical regions of the world, with high morbidity and mortality rates in countries in which it is endemic. In 2021, 247 million cases with 619,000 deaths were reported.[1] Although a malaria vaccine has recently been licensed for children in the most at-risk areas, its efficacy is still considered low and it is unclear whether vaccination will have a significant impact on disease control.[2]

The gold standard methods for the diagnosis of malaria include microscopy and molecular methods. Microscopy depends on the skills and experience of the microscopist, which can vary and sometimes lead to false-negative results, especially when parasite density is low. The test is time-consuming and requires a minimum laboratory structure and trained personnel to prepare and examine blood stains. The molecular method commonly used as the gold standard for the diagnosis of malaria is the real-time polymerase chain reaction.[3] This technique detects the genetic material (DNA or RNA) of the malaria parasite and provides highly sensitive and specific results. However, it demands infrastructure, expensive equipment, and specialized technicians for its execution.

An alternative to these methods is the rapid diagnostic test due to its simplicity, speed, and suitability for on-site testing.[4] This type of test uses antibodies that specifically bind to infection biomarkers and produce a visible line or signal when the target protein is present in the patient's blood.[5] Various biomarkers can be used for malaria diagnosis, including histidine-rich protein 2 (HRP2), which is commonly used in rapid diagnostic tests to detect *Plasmodium falciparum*.[6−9] Despite the practicality of these tests, they are not capable of detecting low parasitemia, which can lead to false-negative results.

Biosensors have shown promise as an alternative for the diagnosis of malaria. In the context of malaria diagnosis, biosensors can be developed to detect malaria-specific antigens or genetic material.[4,5,10,11] Biosensors offer high sensitivity and detection limits and allow the detection of low parasite

Received: May 13, 2024
Revised: June 22, 2024
Accepted: July 4, 2024
Published: July 15, 2024

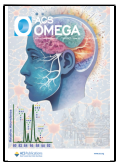

https://doi.org/10.1021/acsomega.4c04543
ACS Omega 2024, 9, 33130−33139

densities or early stages of infection.[12,13] They can also detect malaria biomarkers rapidly and in real-time, enabling rapid diagnosis and timely initiation of treatment. These devices are designed to be portable and hand-held, which makes them suitable for use in resource-limited environments and remote areas with limited access to laboratory facilities.[14,15] The biosensors can be designed to be easy to use and require minimal training. This allows them to be used by medical personnel with varying levels of expertise.

Several electrochemical biosensors are described in the literature for detecting HRP2 protein,[16] and all these methodologies are based on natural antibodies.[5,17,18] These biological detection elements have several advantages and disadvantages in terms of robustness, price, and mass production.[19,20] However, plastic antibodies such as MIPs could overcome these limitations. These plastic antibodies use a target molecule as a model in the formation of a polymeric matrix and, after the template removal, have recognition sites with a format that is complementary to the target molecule, and also the correct orientation of the functional groups, allowing the selective detection of the analyte.[21]

When evaluating an electrochemical sensor platform based on MIP for analyzing target analytes, the most important factors are selectivity, sensitivity, response time, stability, resistance to interference, cost efficiency, scalability, and versatility. MIP-based sensors offer high selectivity and sensitivity with fast response times and resistance to interference thanks to customized cavities. They are stable, reusable, cost-effective, scalable and versatile in various applications.[21−24] This is a significant advantage over assays using antibodies that are more sensitive to temperature and other storage parameters.[25,26]

There are some alternatives for the formation of the polymer matrix in imprinting assays. The most notable of these is polymerization by chemical processes, which has the disadvantage of allowing less control over polymer matrix properties such as thickness and uniformity.[27] Electropolymerization (ELP) is a simple film formation process that provides control over electrical properties, film thickness, polymerization uniformity and has good carrier adhesion.[28−31]

In this study, we used methylene blue as a monomer to create protein-printed cavities on the surface of poly(methylene blue) (PMB) using the ELP technique. The remarkable advantage of this polymer is its electroactivity, which enables the direct detection of proteins without the need for a liquid redox probe. Consequently, the detection of proteins can be performed directly on the electrode surface.

As such, this study aimed to produce MIPs using the ELP technique and methylene blue as a monomer to detect HRP2. The construction of the sensor and the electrochemical detection of proteins in the buffer, as well as selectivity assays, are presented and discussed in this research.

2. MATERIALS AND METHODS

2.1. Reagents. All the solutions were prepared in Milli-Q ultrapure water (conductivity <0.1 μS cm^{-1}). The reagents included 0.1 M potassium chloride (KCl), 0.01 M 3,4-ethylenedioxythiophene (EDOT) diluted in 0.1 M KCl, 0.5 mg mL^{-1} methylene blue (MB), phosphate-buffered saline (PBS) composed of 140 mmol L^{-1} NaCl, 10 mmol L^{-1} phosphate buffer, and 3 mmol L^{-1} KCl, 0.1 M chloroauric acid ($HAuCl_4$) diluted in 1 M ammonium chloride (NH_4Cl), 5 mM potassium ferricyanide ($[K_3[Fe(CN)_6]$) and potassium ferrocyanide ($K_4[Fe(CN)_6]$) and bovine serum albumin (BSA), which were purchased from Sigma-Aldrich. 500 μg mL^{-1} Proteinase K was obtained from VWR, and 0.5 mol L^{-1} oxalic acid, was obtained from Merck. The HRP2 recombinant protein was provided by Leônidas and Maria Deane Institute − ILMD/Fiocruz Amazônia. The interferents used in the selectivity test were human IgG, creatinine, and the recombinant protein lactate dehydrogenase from *Plasmodium vivax* (*Pv*LDH) provided by ILMD.

2.2. Apparatus. A potentiostat/galvanostat (Metrohm Autolab) equipped with an FRA module controlled by NOVA 2.1.6 software was used to perform the electrochemical analysis. The electrodes used were commercial screen-printed carbon electrodes (C-SPE) (Metrohm DropSens, C-110), consisting of carbon and silver working and counter electrodes for the reference electrodes and silver electrical contacts. The diameter of the working electrode was 4 mm. A portable control box (BioTID) provided the connection between the C-SPEs and the potentiostat.

The Raman spectrum of the construction of the MIPs and NIPs on the carbon electrode was recorded using a Raman imaging microscope (Thermo Scientific DXR3xi) using 10 mW at a wavelength of 532 nm for excitation and a slit aperture of 50 μm. The collected data were analyzed using OMNIC software (Thermo Fisher Scientific). The SEM was performed using a high-resolution field emission scanning electron microscope (JEOL JSM 6301 F/Oxford INCAEnergy 350/Gatan Alto 2500).

2.3. Gene Cloning, Protein Expression and Purification of Recombinant HRP2 from *Plasmodium falciparum*. A genomic DNA sample obtained from the *P. falciparum* 3D7 strain served as a template for amplification of exon 2 of the HRP2 gene (Genebank reference: AH002578) using the Sense 5′ AATTCCGCATTTAATAATAACTT 3′ and Antisense 5′ ATTTAATGGCGTAGGCAATGTGT 3′ primers. The PCR product was cloned into the pGEM vector (Promega), followed by transformation of an *Escherichia coli*, DH5α strain, using the constructed plasmid. After selection of the bacterial clones via PCR using the primers described above, the inset was restricted using the enzyme EcoR1 and purified using the DNA gel extraction kit (QIAGEN). Subsequently, the fragment was subcloned into a pGEX-3x plasmid (previously digested with EcoR1) using T4 ligase (Invitrogen) and transformation of *E. coli*, strain TOP 10, by electroporation with the construct. Colonies containing the fragment were selected via PCR. After this step, the plasmid was purified and introduced into an *E. coli* BL21 (DE3) pLysS strain. Protein expression was then induced with IPTG for 3 h at a bacterial density of 0.8 at 600 nm. The protein was purified by extracting the bacterial pellet via ultrasonic lysis and subjected to affinity chromatography with glutathione sepharose resin (Amersham). The protein was eluted by competition with free glutathione in a buffer and the result was analyzed via SDS-PAGE electrophoresis. After expression and purification, a protein of 70 kDa, the expected mass of recombinant HRP2, was detected in SDS-PAGE (Figure S1). This molecular mass is the sum of the amino acids of the HRP2 protein sequence (44 kDa) and the tail of the glutathione S-transferase (GST) present in the expression plasmid (26 kDa) (Figure S1).

2.4. Electrochemical Measurements. All CV and SWV measurements were performed in triplicate by incubating 70 μL of 5.0 mmol L^{-1} $[Fe(CN)_6]^{3-}$ and 5.0 mmol L^{-1} $[Fe(CN)_6]^{4-}$ in PBS buffer pH 7.4 on the C-SPE surface in

https://doi.org/10.1021/acsomega.4c04543
ACS Omega 2024, 9, 33130−33139

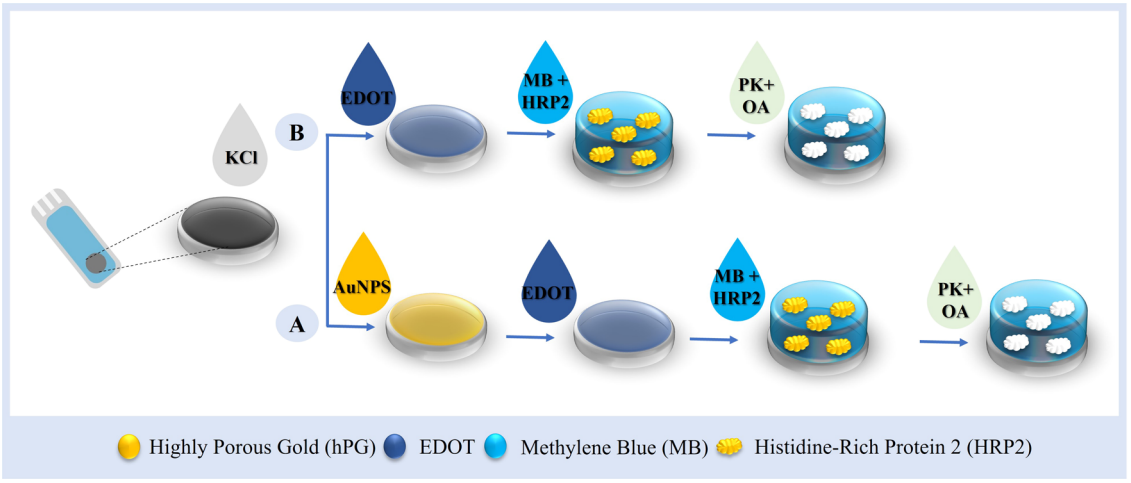

Figure 1. MIP construction methodology. (A) Construction using hPG electrodeposition, followed by the PEDOT layer; (B) Construction using only one layer of PEDOT.

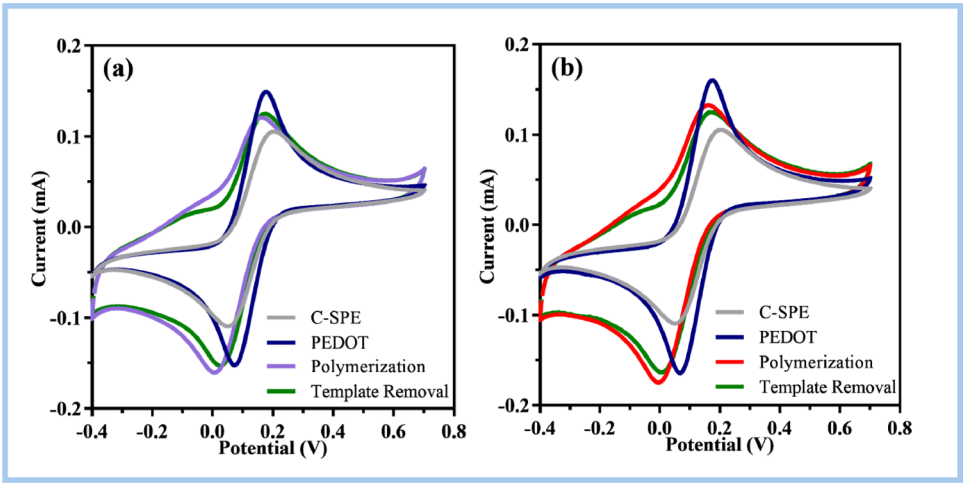

Figure 2. (a) CV measurement of MIPs: electrode after pretreatment (gray), after a layer of PEDOT (blue), after EPL of MIPs (purple), and after removal (green); (b) CV measurement of NIPs: electrode after pretreatment (gray), after the PEDOT layer (blue), after EPL of NIPs (red) and after removal (green). Readings were performed using a 5 mM redox solution $[Fe(CN)_6]^{3-/4-}$ prepared in 0.01 M PBS pH 7.4.

the case of CV measurements. For the SWV measurements, only 0.1 M KCl was used. For the CV assays, potentials were scanned from −0.7 to +1.1 V at a scan rate of 50 mVs^{-1} and, for SWV, a potential sweep from −0.7 to +0.2 V was used with a frequency of 5 Hz and a step height of 5 mV.

Calibration curves were generated using SWV measurements for HRP2 protein ranging from 64 pg mL^{-1} to 5 μg mL^{-1} in PBS buffer pH 7.4. Aliquots of 5 μL of each standard were incubated for 20 min on the working surface of the C-SPE.

Selectivity studies were performed via competitive and separated solutions methods. In a competitive assay between HRP2 at a concentration of 32 ng mL^{-1} and other interfering species. The interferents selected for this purpose were human IgG (diluted to 1:1000), creatinine (5 μg mL^{-1}), or *Pv*LDH (0.032 μg mL^{-1}). All these compounds were prepared in PBS buffer pH 7.4.

For the separated solution method, the interferents selected for this purpose were human IgG (diluted to 1:1000), creatinine (5 μg mL^{-1}) or *Pv*LDH (0.032 μg mL^{-1}), and HRP2 (32 ng mL^{-1}) were incubated during 20 min in the MIP sensor. Determination of HRP2 in the samples was performed by SWV measurements. HPR2 was prepared in 1000-fold diluted synthetic serum ranging from 64 pg mL^{-1} to 5 μg mL^{-1}.

2.5. Molecular Imprinted Assembly. The construction of an HRP2 MIP on C-SPE followed the scheme shown in Figure 1. To ensure optimal stability and the required electrical and chemical properties, a pretreatment step was performed due to the insufficient stability of the carbon substrate. The initial pretreatment included a thorough cleaning step to facilitate the electrochemical oxidation of all the materials and impurities on the carbon surface of the working electrode (WE). This pretreatment was performed using chronoamperometry (CA), with a potential of +1.7 V applied for a duration of 200 s with a 0.1 M KCl solution. The second step focused on improving the electrical response of the biosensor and involved the ELP of EDOT to produce poly(3,4-ethylenedioxythiophene) (PEDOT). The ELP was performed using CA, +1 V for 10 s in PBS buffer pH 7.4. This polymer is known for being one of the most stable conducting polymers. Moreover, the sulfur groups in PEDOT facilitate better bonding of the polymer PMB to the electrode surface in the following stage.[32]

https://doi.org/10.1021/acsomega.4c04543
ACS Omega 2024, 9, 33130−33139

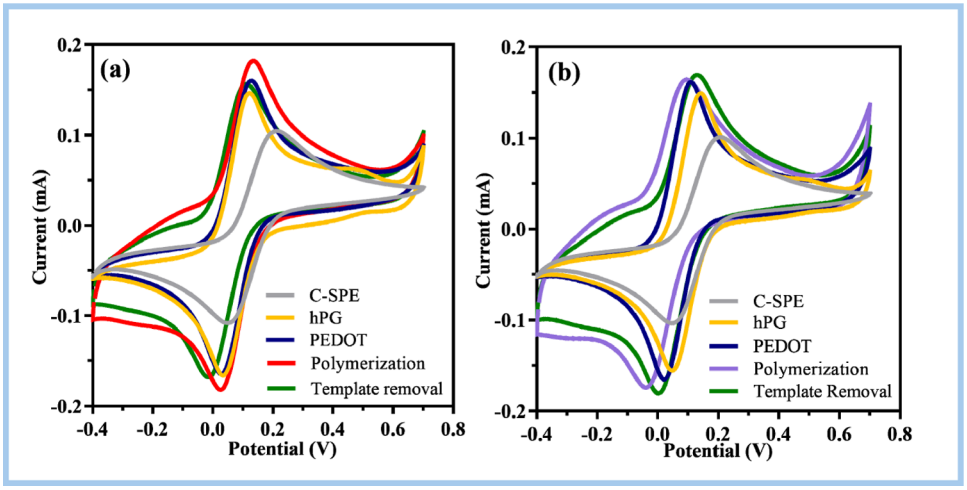

Figure 3. (a) CV measurement of MIPs: electrode after pretreatment (gray), after hPG electrodeposition (yellow), after PEDOT layer (blue), after EPL of MIP (red), and after removal (green); (b) CV measurement of NIPs: electrode after pretreatment (gray), after hPG electrodeposition (yellow), after PEDOT layer (blue), after EPL of NIPs (purple) and after removal (green). Measurements were performed using a 5 mM redox solution $[Fe(CN)_6]^{3-/4-}$ prepared in 0.01 M PBS pH 7.4.

The MIP films were prepared by covering the WE area of the C-SPE with 70 μL of 0.5 mg mL^{-1} MB and 0.1 mg mL^{-1} of recombinant protein HRP2 diluted in 0.01 M pH 7.4 PBS. Polymerization was performed using CV between −0.7 and +1.1 V at a scan rate of 20 mV s^{-1} for 10 cycles. The resulting film was washed thoroughly with PBS buffer. The protein was then removed by adding 500 μg mL^{-1} proteinase K for 2 h in a humidified chamber, followed by a further 1 h incubation in 0.5 mol L^{-1} oxalic acid (Figure 1A,1B). In parallel, the control NIP was prepared in the same way as the MIP, but without the target molecule.

To understand the effects of the nanoparticles on the electrochemical analysis performance of the sensor, an additional was introduced step. Electrolytic deposition of nanoparticles of gold (hPG) was performed on the C-SPE surface (Figure 1A). For this purpose, two CA cycles were performed in 0.1 M $HAuCl_4$ diluted in 1 M NH_4Cl, −0.7 and −1.5 V for 10 s.

3. RESULTS AND DISCUSSION

3.1. Electrochemical Follow-up of the Biosensing Assembly. Figure 2 shows the electrochemical follow-up of the MIP and NIP deposited on the surface of the C-SPE electrode. Both electrodes showed an increase in net current after the ELP of the PEDOT on the C-SPE surface. This pretreatment step improved the conductivity of the electrode by adding a highly conductive polymer layer to the carbon support and increasing the roughness and number of reactive sites on the surface of the electrodes. For this purpose, the electrodes were treated using CA at +1.0 V with a 0.01 M EDOT solution for 10 s. The following step consists of molecular imprinting of the target protein. The PEDOT, which has a thiol group, is expected to interact with MB and form a covalent bond with the MIP/NIP film, ensuring that the imprinted polymer layer is firmly bonded to the WE.

In method A (Figure 2b), the ELP of MB mixed with HRP2 via the CV technique led to a slight current reduction in the MIP-based polymer film. Both NIP and MIP induced a slightly nonconductive but electroactive film on the modified C-SPE electrode surface. This was evidenced in the CV data by the decrease in the net currents (Figure 2a,b). The next step consists of in to remove the protein from the polymer matrix to form the imprint sites in the MIP sensor. The modified C-SPEs were incubated in proteinase K solution, a highly active and stable enzyme that exhibits low cleavage specificity and broad cleavage specificity. Moreover, after treatment with the enzyme, some C-SPEs showed unstable electrical responses after successive measurements, which could be related to the adsorption of the proteinase in the polymer matrix. An additional step was therefore added. A further incubation with oxalic acid was performed for 2 h to ensure proper extraction of the HRP2 from the polymer. After this step, the peak oxidation current increased slightly in the MIP (Figure 2a), while it decreased in the NIP (Figure 2b). The slight increase in current in the MIP is to be expected as the absence of the protein facilitates electron transfer.

To understand the impact of the presence of the nanomaterials on the analytical performance of the sensor, a highly porous gold (hPG) layer was electrodeposited on the bare C-SPE surface prior to coating with PEDOT and MIP/NIP (Figure 3). This step led to a significant increase in current and a reduction in the peak current gap. These observations can be attributed to the high conductivity of hPG, which is favored by its porous morphology and the presence of high salt concentrations.[33] Subsequently, the deposition of the PEDOT layer on the modified electrode was carried out using CA. As described above, the incorporation of PEDOT served as a crucial link between the hPG and PMB and established a covalent sulfur bond. This step resulted in a slight increase in net current compared to the PEDOT layer, as shown in Figure 3. This slight increase could be due to the inherently conductive nature of the previous layer, hPG.

In contrast to the previous method, an increase in current was observed after ELP of MIP and NIP using MB as the monomer, which was slightly more pronounced in the MIP-based sensor. This event could be due to the morphological changes in the polymer promoted by the hPG layer. After treatment with proteinase K and oxalic acid, a decrease in net current was observed in the MIP sensor, which is due to the conductive properties of its surface.[34] After extraction of the HRP2, the opposite behavior occurs, as the presence of cavities reduces the amount of polymer and thus the current (Figure

https://doi.org/10.1021/acsomega.4c04543
ACS Omega 2024, 9, 33130−33139

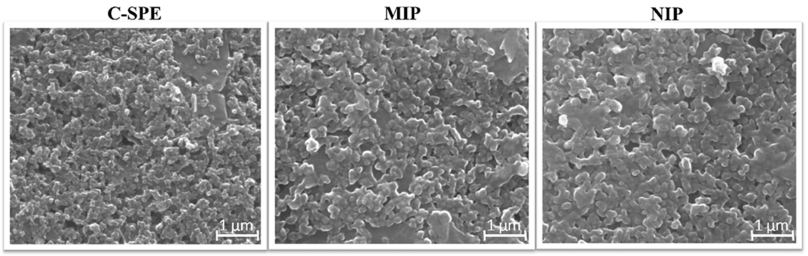

Figure 4. SEM images of the C-SPE-, MIP-, and NIP-based sensors at ×100,000.

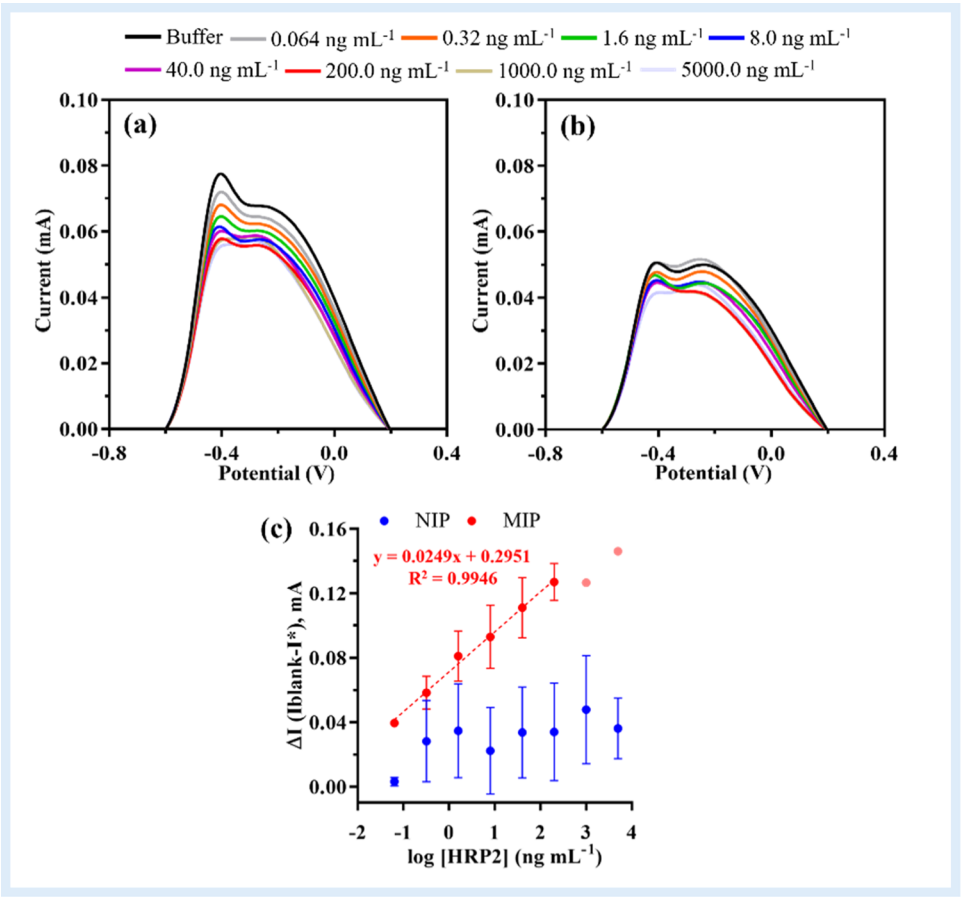

Figure 5. (a) SWV demonstrating the calibration curve of MIPs produced using method "B" in 0.01 M pH 7.4 PBS; (b) SWV demonstrating the calibration curve of NIPs produced by method "B" in 0.01 M pH 7.4 PBS; (c) Calibration curve of the logarithmic concentration of HRP2 protein as a function of current. The salmon-colored dots correspond to the concentration points taken from the curve. Readings were performed in 0.1 M KCl, with a scan rate of 25 mV s^{-1}.

3). In the NIP material, the current is equal to that of the polymer matrix, which is to be expected as there are no voids in the polymer surface.

3.2. Biosensor Surface Characterization. *3.2.1. Raman Spectroscopy.* The Raman spectra of the carbon WE were recorded for the different stages of electrode modification. Figure S2 shows the layers for the different stages of modification of the buildup of PEDOT/MIP or NIP on the carbon electrode (a) pretreatment (C-SPE), (b) PEDOT, (c) NIP and (d) MIP, after EPL and removal of the template. All Raman bands observed in the spectra are listed in Table S1 with the description of each vibration. Figure S2a shows eight peaks typically found in carbon materials located at D* (1151 cm^{-1}), D (1347 cm^{-1}), G (1578 cm^{-1}), D′ (1616 cm^{-1}), G* (2472 cm^{-1}), D-G′ (2687 cm^{-1}), and D+D′ (2917 cm^{-1}) Raman shifts. These are five known bands (D*, D, D″, G, and D′) in the first-order Raman spectrum and three bands (G*, 2D, and D+D′) in the second-order Raman spectrum that successfully interpret the Raman spectra. The D* band originates from the sp^3 orbital and is similar to the D* band observed in sp^3-rich phases,[35] disordered graphene oxide flakes, and powders.[36] The D band represented arises from the defects and disorders in the carbon lattice and the double resonant processes near the *K* point of the Brillouin zone (BZ) boundary.[37] The G band represented the bond-stretching vibrations of sp^2 hybridization carbon atoms, expressing the C═C stretching of graphitic structures.[37,38] The D″ band is related to the amorphous phase, and its intensity is inversely related to the crystallinity.[37] The D′ band corresponds to an

https://doi.org/10.1021/acsomega.4c04543
ACS Omega 2024, 9, 33130−33139

intravalley resonance with the G band and undergoes splitting due to impurities.[37]

In Figure S2b, the most intense band observed at 1439 cm^{-1} corresponds to the PEDOT and represents the symmetric stretching vibration of the Cα=Cβ bond in a five-membered thiophene ring. This vibration arises in the neutral regions between the localized elementary excitations.[39,40] The absence of a shoulder at about 1449 cm^{-1}, corresponding to the symmetric stretching modes of the benzoic Cα=Cβ components, indicates the presence of quinoid structures. This suggests a conformational transformation of the PEDOT chains from convoluted to linear or extended convoluted configurations.

The bands at 1510 and 1577 cm^{-1} are associated with the thiophene rings in the middle and at the end of the PEDOT chains.[40] These bands are due to the asymmetric stretching vibration of the Cα=Cβ bond. The stretching deformations of the Cβ-Cβ and Cα-Cα bonds between the rings of PEDOT are represented by the bands at 1248 and 1121 cm^{-1}, respectively[41] and symmetric C−S−C deformation is assigned to the band at 849 and 696 cm^{-1}. The bands at 989, 574, and 439 cm^{-1} are assigned to the PEDOT by the deformation of the oxyethylene ring.[42]

Figure S2 shows the structures of PEDOT/NIP (c), PEDOT/NIP TR (c), PEDOT/MIP TR (d) and PEDOT/MIP (d) and illustrates the modification achieved by the PEDOT polymer chain. The observed changes in the band intensity ratio show that the electronic structure of PEDOT is modified by NIP and MIP and their subsequent removal. This confirms the successful modification of the PEDOT layer.

The relative intensity ratio of the D and G bands is a well-studied parameter used to estimate the degree of graphitization and the presence of defects in carbonaceous materials. It serves as a valuable measurement for evaluating the number of defects. The data extracted from the Raman spectra of the different materials, listed in Table S2, provided the I_D and I_G peak values. The initial oxidized carbon material showed an I_D/I_G ratio of 0.94. After electropolymerization of the PEDOT, this ratio decreased to 0.81, but after preparation of NIP, MIP, and the subsequent removal, the I_D/I_G ratio increased slightly to 1.01. Overall, the Raman spectra confirmed the successful chemical modification of the sensor surface. The effectiveness of the modification was further evaluated by examining the resulting analytical properties.

3.2.2. SEM Analysis. The SEM analysis of the C-SPE, MIP, and NIP materials is shown in Figure 4.

In the SEM images, the presence of polymers in the MIP and NIP-based materials is evident, showing an increase in the size of the structures present on the surface when compared to the bare C-SPE. However, the presence of imprints is not obvious. One possible explanation is related to the very rough surface of the C-SPE, which does not allow visualization of the cavities on the MIP surface. Another possible explanation could be related to the resolution limits of the equipment, which may not be able to detect differences in a very small nanometer range.

3.3. Analytical Performance of the Biosensor. *3.3.1. Calibration Curve in Buffer.* The mechanism of detection using MIPs relies on the selective recognition and binding of target molecules by the MIP's specific binding sites, which results in a measurable change used for the detection and quantification of the protein HRP2 using the SWV technique. Figure 5 shows the calibration curve of the MIP and NIP sensors in the buffer. Since the polymer is electroactive, no liquid redox probe is needed for the electrochemical measurements. The profile of the SWV diagram of the MIPs and NIPs developed shows two peaks. However, only the peak at −0.4 V was analyzed because it corresponds to the PMB oxidation peak, as reported by Esokkiya et al.[43] who developed a sensor to detect acrylamide by modifying glassy carbon electrodes with methylene blue using EPL. Differential pulse voltammetry analysis showed the same profile as in the present study, but with a different potential range because the authors used reference electrodes with a different composition.[43] Overall, the SWV measurements showed that the peak current decreased with the increasing concentration of HRP2.

Calibration curves were established based on binding assays of MIPs and NIPs to the recombinant protein diluted in 0.01 M pH 7.4 PBS. The resulting calibration data were monitored with SWV, and the current (mA) was plotted against the logarithm of the HRP2 concentration (Figure 5). The MIP sensor showed the broadest linear response from 0.064 to 200 ng mL^{-1}, with an average slope of 0.0249 mA/decade, detection limit (LD) 0.43 ± 0.026 pg mL^{-1}, R^2 of 0.9948, and low standard deviations (less than 10%). This indicates that the cavities were correctly formed and complementary to the template molecule. The NIPs showed randomness without straight line formation and high standard deviations, which may be due to nonspecific adsorption to the surface of the polymer (Figure 5c). Recent studies using biosensors to detect malaria used lower detection limits than those in the present work.[44,45] However, these assays are more complex and use natural antibodies as the detection layer. Moreover, the LD obtained here is likely to be much lower than that obtained with classical methods such as rapid tests and enzyme immunoassay.[8,46] Dip Gandarilla et al.[7] developed an immunosensor for the detection of HRP2 that achieves a limit of detection (LOD) of 2.8 ng mL^{-1}. In the same study, a comparison was made with an enzyme-linked immunosorbent assay (ELISA), which yielded an LOD of 5.5 ng mL^{-1}.

In addition, we tested a different approach to understand the effects of hPG on the analytical performance of the MIP sensor. Under these conditions, a prominent redox peak appears near −0.2 V and the current values were used to generate the calibration curve (Figure S3). The resulting calibration data were monitored with SWV, and the current (mA) was plotted against the logarithm of the HRP2 concentration (Figure S3). In general, the SWV measurements showed that as the HRP2 concentration increased, the peak anodic current decreased. The MIP sensor showed the broadest linear response from 0.064 to 5000 ng mL^{-1}, and average slope of 0.0039 mA/decade. The NIP showed a random response for the same concentration range.

Compared to the biosensor prepared in the absence of hPG (Figure 1), the slope was almost 10 times lower, indicating that the presence of hPG did not favor the analytical response of the sensor. It was expected that the deposition of hPG would increase the sensitivity of the sensor, since the particles of this gold salt would increase the contact area and conductivity of the electrode surface, making the changes occurring on this surface more noticeable, as reported in other work.[46−48] However, the irregular deposition of hPG might have affected the formation of the PMB polymer layer, resulting in complementary cavities in the target molecule. The irregular deposition of the gold layer may be caused by various factors,

https://doi.org/10.1021/acsomega.4c04543
ACS Omega 2024, 9, 33130−33139

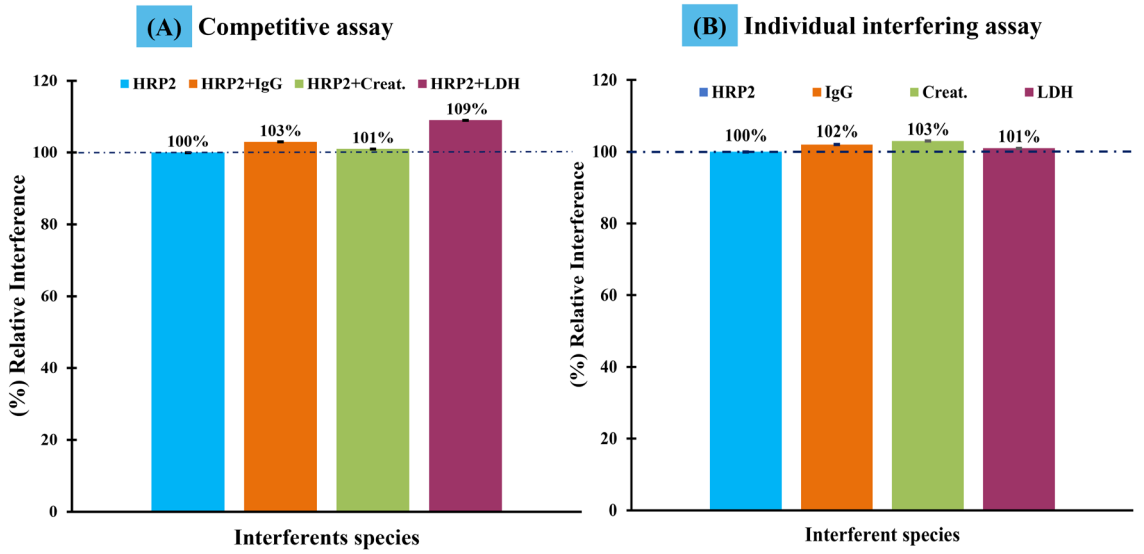

Figure 6. Selectivity study using the competitive (A) and individual interfering (B) solutions. The interferents were human IgG, creatinine, and *Pv*LDH.

such as the positive or negative influence of the supporting electrolytes on the formation of layers by electrodeposition.

3.3.2. Calibration Curve in FBS. In order to test a real application of the biosensor, a calibration with FBS was carried out. The data obtained is shown in Figure S4. For this purpose, the biosensor was stabilized with human serum and then incubated with spiked serum samples with HRP2 concentrations from 0.064 to 5000.0 ng mL^{-1} diluted in FBS (1:1000, in 0.01 M PBS pH 7.4). The measurements were performed without the redox probe, as the PMB had electroactive properties.

The SWVs recorded for the different HRP2 concentrations in diluted FBS and the corresponding plot indicating the correlation between peak current and HRP2 concentration are shown in Figure S4. The plot obtained from the SWV showed a gradual decrease in current with increasing HRP2 concentration for the MIP sensor and a random behavior for the NIP (Figure S3a and S3b). However, when comparing the slope of this calibration with that in the buffer (Figure 5), a lower slope value was observed, which can be attributed to the complexity of the serum samples. Overall, the gradual decrease in current in the electrochemical profile of the electrodes as a function of protein concentration indicates the formation of complementary cavities in the MIPs when analyzed with SWV (Figure S3a). Such behavior was not observed for the NIPs, suggesting randomness of the electrochemical response when incubated with different protein concentrations (Figure S3b). The MIP sensor exhibited a slope of 0.0017 mA/decade and an LLLR of 0.32 ng mL^{-1}.

3.3.3. Selectivity Study. Selectivity tests were accomplished to evaluate the ability of the sensor to distinguish the HRP2 protein from other species in biological samples such as serum. A competitive and a pure interference analysis were performed to evaluate the selectivity of the MIP-based sensor. Chemical compounds that could be present in serum samples were involved in the tests. These included human IgG, creatinine, and PvLDH, which resulted in interference of 1, 3, and 9% respectively in the competitive test (Figure 6A). The higher interference effect was observed when using the PvLDH protein, a recombinant protein that shares regions with the target protein of the expression plasmid used to produce both antigens.

Figure 6B shows the selectivity study for the case where each compound is incubated on the MIP sensor surface for 20 min. Fortunately, no relevant interference effect was detected after the electrochemical measurements.

These results demonstrate the very good selectivity properties of the HRP2 MIP-based sensor, which has a high affinity to the target molecule and not to a competing biomarker that causes selective binding to the MIP surface. Together with a sensitive and accurate response, the results are very promising for the detection of HRP2 in real biological samples.

4. CONCLUSIONS

In this study, we demonstrate the novel production of a new MIP for malaria detection. The results presented here demonstrate the possibility of electrochemical detection of malaria using the PMB polymer, which has the advantage of being electroactive and conductive, reproducible, and more sensitive than the classical methods for malaria diagnosis. The study shows that this type of sensor fabrication is feasible and can be improved to achieve lower detection limits. By using the MIP technique, we can eliminate the use of antibodies for malaria antigen detection, which has excellent ethical and economic advantages, such as eliminating the use of animals and greater stability at high temperatures due to the stability of PMB, this also allows direct detection of the electrochemical signal without a redox solution.

■ ASSOCIATED CONTENT

Supporting Information

The Supporting Information is available free of charge at https://pubs.acs.org/doi/10.1021/acsomega.4c04543.

Analysis of HRP2 recombinant protein purification using SDS-PAGE (15%). M: Molecular weight marker BLUeye Prestained Protein Ladder 1−3: Different elutions of HPR (Figure S1). Raman spectra of several layers of the several stages of modification of the assembly of the PEDOT/MIP or NIP on the carbon electrode. (a)

https://doi.org/10.1021/acsomega.4c04543
ACS Omega 2024, 9, 33130−33139

Pretreatment, (b) PEDOT, (c) NIP and NIP after template removal (TR), and (d) MIP and MIP after TR (Figure S2). (a) SWV demonstrating the calibration curve of MIPs produced by method "A", in 0.01 M pH 7.4 PBS; (b) SWV demonstrating the calibration curve of NIPs produced by method "A" in 0.01 M pH 7.4 PBS; (c) Calibration curve of the logarithmic concentration of HRP2 protein as a function of current. Readings were performed in 0.1 M KCl, with a scan rate of 25 mV s^{-1} (Figure 3). SWV demonstrating the calibration curve of MIPs produced using method "B", in FBS; SWV demonstrating the calibration curve of NIPs produced using method "b", in FBS; (c) Calibration curve of the logarithmic concentration of HRP2 protein as a function of current. Readings were performed in 0.1 M KCl, with a scan rate of 25 mV s^{-1} (Figure S4) Analytical data extracted from the collected Raman spectra of the PEDOT, NIP and MIP layers (Table S1) (PDF)

AUTHOR INFORMATION

Corresponding Authors

Walter Ricardo Brito − *Programa de Pós-graduação em Biotecnologia da Universidade Federal do Amazonas - UFAM, Manaus, AM 69077-000, Brazil; Departamento de Química, Universidade Federal do Amazonas, Manaus, AM 69077-000, Brasil; LABEL − Central Analítica, Universidade Federal do Amazonas, Manaus, AM 69077-000, Brazil;* orcid.org/0000-0002-6493-0237; Email: wrbrito@ufam.edu.br

Felismina T. C. Moreira − *CIETI-LabRISE, Instituto Superior de Engenharia do Porto (ISEP), Porto 4249-015, Portugal;* orcid.org/0000-0003-4237-8952; Email: ftm@isep.ipp.pt

Authors

Juliane Corrêa Glória − *Programa de Pós-graduação em Biotecnologia da Universidade Federal do Amazonas - UFAM, Manaus, AM 69077-000, Brazil; Instituto Leônidas e Maria Deane (ILMD) and Programa de Pós-graduação em Biologia da Interação Patógeno-Hospedeiro do Instituto Leônidas e Maria Deane (ILMD), Fundação Oswaldo Cruz (FIOCRUZ), Manaus, AM 69057-070, Brazil*

Daniela S. Oliveira − *CIETI-LabRISE, Instituto Superior de Engenharia do Porto (ISEP), Porto 4249-015, Portugal*

Ariamna Dip Gandarilla − *Departamento de Química, Universidade Federal do Amazonas, Manaus, AM 69077-000, Brasil; LABEL − Central Analítica, Universidade Federal do Amazonas, Manaus, AM 69077-000, Brazil*

Yonny Romaguera Barcelay − *Departamento de Química, Universidade Federal do Amazonas, Manaus, AM 69077-000, Brasil; CEMMPRE, Departamento de Engenharia Química, Universidade de Coimbra, 3030-790 Coimbra, Portugal*

Luis André Morais Mariúba − *Programa de Pós-graduação em Biotecnologia da Universidade Federal do Amazonas - UFAM, Manaus, AM 69077-000, Brazil; Instituto Leônidas e Maria Deane (ILMD) and Programa de Pós-graduação em Biologia da Interação Patógeno-Hospedeiro do Instituto Leônidas e Maria Deane (ILMD), Fundação Oswaldo Cruz (FIOCRUZ), Manaus, AM 69057-070, Brazil; Programa de Pós-graduação em Imunologia Básica e Aplicada, Instituto de Ciências Biológicas, Universidade Federal do Amazonas (UFAM), Manaus, AM 69067-00, Brazil*

Paulo Afonso Nogueira − *Instituto Leônidas e Maria Deane (ILMD) and Programa de Pós-graduação em Biologia da Interação Patógeno-Hospedeiro do Instituto Leônidas e Maria Deane (ILMD), Fundação Oswaldo Cruz (FIOCRUZ), Manaus, AM 69057-070, Brazil; Programa de Pós-graduação em Imunologia Básica e Aplicada, Instituto de Ciências Biológicas, Universidade Federal do Amazonas (UFAM), Manaus, AM 69067-00, Brazil*

Complete contact information is available at: https://pubs.acs.org/10.1021/acsomega.4c04543

Author Contributions

◆J.C.G. and D.S.O. contributed equally to this work.

Notes

The authors declare no competing financial interest.

ACKNOWLEDGMENTS

This work was partially supported by the Portuguese Foundation for Science and Technology (FCT), through grants UIDB/04730/2020; UIDP/04730/2020 and FCT - CAPES/FCT − Edital n ° 34/2018.

REFERENCES

(1) https://www.who.int/news-room/fact-sheets/detail/malaria, https://www.who.int/news-room/fact-sheets/detail/malaria, 2023.

(2) Landier, J.; Parker, D. M.; Thu, A. M.; Carrara, V. I.; Lwin, K. M.; Bonnington, C. A.; Pukrittayakamee, S.; Delmas, G.; Nosten, F. H. The role of early detection and treatment in malaria elimination. *Malar. J.* **2016**, *15*, No. 363.

(3) Johnston, S. P.; Pieniazek, N. J.; Xayavong, M. V.; Slemenda, S. B.; Wilkins, P. P.; da Silva, A. J. PCR as a confirmatory technique for laboratory diagnosis of malaria. *J. Clin. Microbiol.* **2006**, *44* (3), 1087−1089.

(4) Ragavan, K. V.; Kumar, S.; Swaraj, S.; Neethirajan, S. Advances in biosensors and optical assays for diagnosis and detection of malaria. *Biosens. Bioelectron.* **2018**, *105*, 188−210.

(5) Hemben, A.; Ashley, J.; Tothill, I. E. Development of an Immunosensor for PfHRP 2 as a Biomarker for Malaria Detection. *Biosensors* **2017**, *7* (3), No. 28.

(6) Bhardwaj, N.; Ahmed, M. Z.; Sharma, S.; Srivastava, B.; Pande, V.; Anvikar, A. R. Clinicopathological study of potential biomarkers of *Plasmodium falciparum* malaria severity and complications. *Infect., Genet. Evol.* **2020**, *77*, No. 104046, DOI: 10.1016/j.meegid.2019.104046.

(7) Dip Gandarilla, A. M.; Regiart, M.; Bertotti, M.; Gloria, J. C.; Mariuba, L. A. M.; Brito, W. R. One-step enzyme-free dual electrochemical immunosensor for histidine-rich protein 2 determination. *RSC Adv.* **2021**, *11* (1), 408−415.

(8) Kifude, C. M.; Rajasekariah, H. G.; Sullivan, D. J.; Stewart, V. A.; Angov, E.; Martin, S. K.; Diggs, C. L.; Waitumbi, J. N. Enzyme-linked immunosorbent assay for detection of *Plasmodium falciparum* histidine-rich protein 2 in blood, plasma, and serum. *Clin. Vaccine Immunol.* **2008**, *15* (6), 1012−1018.

(9) Liang, J. X.; Bunck, D. N.; Mishra, A.; Hong, S.; Idso, M. N.; Heath, J. R. Inhibition of heme sequestration of histidine-rich protein 2 using multiple epitope-targeted peptides. *J. Pept. Sci.* **2019**, *25* (9), No. e3203.

(10) Krampa, F. D.; Aniweh, Y.; Kanyong, P.; Awandare, G. A. Recent Advances in the Development of Biosensors for Malaria Diagnosis. *Sensors* **2020**, *20* (3), No. 799.

(11) Baptista, V.; Peng, W. K.; Minas, G.; Veiga, M. I.; Catarino, S. O. Review of Microdevices for Hemozoin-Based Malaria Detection. *Biosensors* **2022**, *12* (2), No. 110.

(12) Lu, L. L.; Zeng, R. J.; Lin, Q. Y.; Huang, X.; Tang, D. P. Cation Exchange Reaction-Mediated Photothermal and Polarity-Switchable

Photoelectrochemical Dual-Readout Biosensor. *Anal. Chem.* **2023**, *95* (44), 16335−16342.
(13) Wu, D.; Tang, D. P. Recent advances on portable photoelectrochemical biosensors for diagnostics. *Electroanalysis* **2023**, *35* (12), No. e202300265.
(14) Zeng, R. J.; Qiu, M. H.; Wan, Q.; Huang, Z. S.; Liu, X. L.; Tang, D. P.; Knopp, D. Smartphone-Based Electrochemical Immunoassay for Point-of-Care Detection of SARS-CoV-2 Nucleocapsid Protein. *Anal. Chem.* **2022**, *94*, 15155−15161.
(15) Yu, Z. C.; Gong, H. X.; Xu, J. H.; Li, Y. X.; Zeng, Y. Y.; Liu, X. L.; Tang, D. P. Exploiting Photoelectric Activities and Piezoelectric Properties of NaNbO Semiconductors for Point-of-Care Immunoassay. *Anal. Chem.* **2022**, *94* (7), 3418−3426.
(16) Nate, Z.; Gill, A. A. S.; Chauhan, R.; Karpoormath, R. Recent progress in electrochemical sensors for detection and quantification of malaria. *Anal. Biochem.* **2022**, *643*, No. 114592.
(17) Markwalter, C. F.; Jang, I. K.; Burton, R. A.; Domingo, G. J.; Wright, D. W. Biolayer interferometry predicts ELISA performance of monoclonal antibody pairs for *Plasmodium falciparum* histidine-rich protein 2. *Anal. Biochem.* **2017**, *534*, 10−13.
(18) Paul, K. B.; Kumar, S.; Tripaty, S.; Singh, V.; Vanjari, S. R. K.; Singh, S. G. Highly-sensitive label-free differential pulse voltammetric immunosensor for diagnosis of infectious diseases based on electrospun copper doped ZnO nanofiber biosensing platform. *Procedia Technol.* **2017**, *27*, 219−220.
(19) Gao, Y.; Zeng, Y. Y.; Liu, X. L.; Tang, D. P. Liposome-Mediated In Situ Formation of Type-I Heterojunction for Amplified Photoelectrochemical Immunoassay. *Anal. Chem.* **2022**, *94* (11), 4859−4865.
(20) Gao, Y.; Li, M. J.; Zeng, Y. Y.; Liu, X. L.; Tang, D. P. Tunable Competitive Absorption-Induced Signal-On Photoelectrochemical Immunoassay for Cardiac Troponin I Based on Z-Scheme Metal-Organic Framework Heterojunctions. *Anal. Chem.* **2022**, *94*, 13582−13589.
(21) Frasco, M. F.; Truta, L.; Sales, M. G. F.; Moreira, F. T. C. Imprinting Technology in Electrochemical Biomimetic Sensors. *Sensors* **2017**, *17* (3), No. 523.
(22) Wang, L.; Pagett, M.; Zhang, W. Molecularly imprinted polymer (MIP) based electrochemical sensors and their recent advances in health applications. *Sens. Actuators Rep.* **2023**, *5*, No. 100153.
(23) Ahmad, O. S.; Bedwell, T. S.; Esen, C.; Garcia-Cruz, A.; Piletsky, S. A. Molecularly Imprinted Polymers in Electrochemical and Optical Sensors. *Trends Biotechnol.* **2019**, *37* (3), 294−309.
(24) Mezhuev, Y. O.; Vorobev, I. Y.; Plyushchii, I. V.; Krivoborodov, E. G.; Artyukhov, A. A.; Motyakin, M. V.; Luss, A. L.; Ionova, I. S.; Kovarskii, A. L.; Derevnin, I. A.; Dyatlov, V. A.; Alekperov, R. A.; Toropygin, I. Y.; Volkov, M. A.; Shtilman, M. I.; Korshak, Y. V. Chemical Oxidative Polymerization of Methylene Blue: Reaction Mechanism and Aspects of Chain Structure. *Polymers* **2021**, *13* (13), No. 2188.
(25) Kirk, R. E.; Othmer, D. F. Kirk-Othmer encyclopedia of chemical technology. *Chem. Ind.* **1965**, *11*, 457.
(26) Albertini, A.; Lee, E.; Coulibaly, S. O.; Sleshi, M.; Faye, B.; Mationg, M. L.; Ouedraogo, K.; Tsadik, A. G.; Feleke, S. M.; Diallo, I.; Gaye, O.; Luchavez, J.; Bennett, J.; Bell, D. Malaria rapid diagnostic test transport and storage conditions in Burkina Faso, Senegal, Ethiopia and the Philippines. *Mala. J.* **2012**, *11*, No. 406.
(27) Kaplan, I. H.; Dagci, K.; Alanyalioglu, M. Nucleation and Growth Mechanism of Electropolymerization of Methylene Blue: The Effect of Preparation Potential on Poly(methylene blue) Structure. *Electroanalysis* **2010**, *22* (22), 2694−2701.
(28) Mello, R.; Hümmelgen, I. Ohmic contacts between sulfonated polyaniline and metals. *J. Solid State Electrochem.* **2001**, *5* (7), 546−549.
(29) Stilwell, D. E.; Park, S. M. electrochemistry of conductive polymers. 6. Degradation reaction-kinetics of polyaniline studied by rotating-ring-disk electrode techniques. *J. Electrochem. Soc.* **1989**, *136* (3), 688−698.
(30) Meneguzzi, A.; Ferreira, C. A.; Pham, M. C.; Delamar, M.; Lacaze, P. C. Electrochemical synthesis and characterization of poly(5-amino-1-naphthol) on mild steel electrodes for corrosion protection. *Electrochim. Acta* **1999**, *44* (12), 2149−2156.
(31) Gandarilla, A. M. D.; Matos, R. S.; Barcelay, Y. R.; da Fonseca Filho, H. D.; Brito, W. R. Molecularly imprinted polymer on indium tin oxide substrate for bovine serum albumin determination. *J. Polym. Res.* **2022**, *29* (5), No. 166.
(32) Pereira, M. V.; Marques, A. C.; Oliveira, D.; Martins, R.; Moreira, F. T. C.; Sales, M. G. F.; Fortunato, E. Paper-Based Platform with an In Situ Molecularly Imprinted Polymer for beta-Amyloid. *ACS Omega* **2020**, *5* (21), 12057−12066.
(33) Moreira, F. T. C.; Sale, M. G. F.; Di Lorenzo, M. Towards timely Alzheimer diagnosis: A self-powered amperometric biosensor for the neurotransmitter acetylcholine. *Biosens. Bioelectron.* **2017**, *87*, 607−614.
(34) Moreira, F. T. C.; Sharma, S.; Dutra, R. A. F.; Noronha, J. P. C.; Cass, A. E. G.; Sales, M. G. F. Smart plastic antibody material (SPAM) tailored on disposable screen printed electrodes for protein recognition: Application to myoglobin detection. *Biosens. Bioelectron.* **2013**, *45*, 237−244.
(35) Nemanich, R. J.; Glass, J. T.; Lucovsky, G.; Shroder, R. E. raman-scattering characterization of carbon bonding in diamond and diamondlike thin-films. *J. Vac. Sci. Technol., A* **1988**, *6* (3), 1783−1787.
(36) Castaño-Guerrero, Y.; Romaguera-Barcelay, Y.; Moreira, F. T. C.; Brito, W. R.; Fortunato, E.; Sales, M. G. F. Poly(Thionine)-Modified Screen-Printed Electrodes for CA 19−9 Detection and Its Properties in Raman Spectroscopy. *Chemosensors* **2022**, *10* (3), No. 92.
(37) Reich, S.; Thomsen, C. Raman spectroscopy of graphite. *Philos. Trans. R. Soc., A* **2004**, *362* (1824), 2271−2288.
(38) Lucchese, M. M.; Stavale, F.; Ferreira, E. H. M.; Vilani, C.; Moutinho, M. V. O.; Capaz, R. B.; Achete, C. A.; Jorio, A. Quantifying ion-induced defects and Raman relaxation length in graphene. *Carbon* **2010**, *48* (5), 1592−1597.
(39) Xu, B. R.; Gopalan, S. A.; Gopalan, A. I.; Muthuchamy, N.; Lee, K. P.; Lee, J. S.; Jiang, Y.; Lee, S. W.; Kim, S. W.; Kim, J. S.; Jeong, H. M.; Kwon, J. B.; Bae, J. H.; Kang, S. W. Functional solid additive modified PEDOT: PSS as an anode buffer layer for enhanced photovoltaic performance and stability in polymer solar cells. *Sci. Rep.* **2017**, *7*, No. 45079.
(40) Jucius, D.; Lazauskas, A.; Grigaliunas, V.; Gudaitis, R.; Guobiene, A.; Prosycevas, I.; Abakeviciene, B.; Andrulevicius, M. Structure and Properties of Dual-doped PEDOT:PSS Multilayer Films. *Mater. Res.* **2019**, *22* (6), No. e20190134.
(41) Garreau, S.; Louarn, G.; Buisson, J. P.; Froyer, G.; Lefrant, S. In situ spectroelectrochemical Raman studies of poly(3,4-ethylenedioxythiophene) (PEDT). *Macromolecules* **1999**, *32* (20), 6807−6812.
(42) Park, H.; Lee, S. H.; Kim, F. S.; Choi, H. H.; Cheong, I. W.; Kim, J. H. Enhanced thermoelectric properties of PEDOT: PSS nanofilms by a chemical dedoping process. *J. Mater. Chem. A* **2014**, *2* (18), 6532−6539.
(43) Esokkiya, A.; Sudalaimani, S.; Kumar, K. S.; Sampathkumar, P.; Suresh, C.; Giribabu, K. Poly(methylene blue)-Based Electrochemical Platform for Label-Free Sensing of Acrylamide. *ACS Omega* **2021**, *6* (14), 9528−9536.
(44) Jain, P.; Chakma, B.; Patra, S.; Goswami, P. Potential Biomarkers and Their Applications for Rapid and Reliable Detection of Malaria. *BioMed Res. Int.* **2014**, *2014*, 1−20.
(45) Dutta, G.; Lillehoj, P. B. An ultrasensitive enzyme-free electrochemical immunosensor based on redox cycling amplification using methylene blue. *Analyst* **2017**, *142* (18), 3492−3499.
(46) He, X. L.; Yuan, R.; Chai, Y. Q.; Shi, Y. T. A sensitive amperometric immunosensor for carcinoembryonic antigen detection with porous nanogold film and nano-Au/chitosan composite as immobilization matrix. *J. Biochem. Biophys. Methods* **2008**, *70* (6), 823−829.

https://doi.org/10.1021/acsomega.4c04543
ACS Omega 2024, 9, 33130−33139

(47) Gao, X.; Zhang, Y.; Wu, Q.; Chen, H.; Chen, Z.; Lin, X. One step electrochemically deposited nanocomposite film of chitosan-carbon nanotubes-gold nanoparticles for carcinoembryonic antigen immunosensor application. *Talanta* **2011**, *85* (4), 1980−1985.
(48) Zhang, C. Y.; Zhang, S.; Jia, Y. L.; Li, Y. Y.; Wang, P.; Liu, Q.; Xu, Z.; Li, X. J.; Dong, Y. H. Sandwich-type electrochemical immunosensor for sensitive detection of CEA based on the enhanced effects of Ag NPs@CS spaced Hemin/rGO. *Biosens. Bioelectron.* **2019**, *126*, 785−791.

https://doi.org/10.1021/acsomega.4c04543
ACS Omega 2024, 9, 33130−33139